PNAS

Main Manuscript for

Ocean eddy compensation regulates feedbacks amplifying ozone-induced Southern Ocean cooling

Travis R. Prochko[a1], Xue Liu[a], Qiuying Zhang[a], Frederic Castruccio[b], Ping Chang[a2], Gokhan Danabasoglu[b], Gaopeng Xu[a], Stephen G. Yeager[b], Clara Deser[b], Pedro DiNezio[c]

[a]Department of Oceanography, Texas A&M University, College Station, TX 77843; [b]National Science Foundation National Center for Atmospheric Research, Boulder, CO 80305; [c]Department of Atmospheric and Oceanic Sciences at the University of Colorado Boulder, Boulder, CO 80309

Corresponding authors: Travis Prochko or Ping Chang

Email: [1]trp2@tamu.edu; [2]ping@tamu.edu

Author Contributions: P.C., F.C., G.D., and S.Y. designed research and simulations; F.C., Q.Z., X.L., S.Y. performed simulations; T.R.P., X.L., and Q.Z. analyzed data; T.R.P. and P.C. wrote the manuscript. F.C., G.D., S.Y., C.D., and P.D. provided comments on manuscript.

Competing Interest Statement: The authors declare no competing interest.

Classification: Physical Sciences; Earth, Atmospheric, and Planetary Sciences

Keywords: Southern Ocean cooling; ocean eddy heat transport; ozone depletion

This PDF file includes:

Main Text
Figures 1 to 7

Abstract

This study extends previous work suggesting that the cooling trend observed in the Southern Ocean over the recent decades was primarily driven by Southern Hemisphere stratospheric ozone depletion and highlights the compensating role of ocean eddy-induced meridional heat transport and meridional overturning circulation in shaping the ozone-driven response. We hypothesize that while the ozone-driven intensification of the westerlies initiates the surface cooling in the Southern Ocean through enhanced equatorward Ekman transport, the persistence and amplification of this cooling depend critically on the extent of oceanic eddy compensation, which regulates wind-driven atmosphere-ocean feedback. Unlike standard low-resolution Earth system models that parameterize eddy heat transport, the high-resolution Community Earth System Model (CESM-HR), which explicitly represents eddies, exhibits much weaker compensation. This allows the wind-driven circulation to dominate the meridional overturning, enhancing upwelling and the northward transport of cooler waters in the Southern Ocean, thereby strengthening the wind-driven atmosphere-ocean feedback and producing a more pronounced Southern Ocean cooling trend that aligns more closely with observations.

Significance Statement

Skillful prediction of climate variations on season-to-decadal timescales is essential for informed decision-making. However, widely used coarse-resolution (~1° horizontal grid spacing) Earth system models systematically fail to reproduce the observed Southern Ocean sea surface temperature (SST) trends over 1980-2020, undermining their predictive capability. We present an unprecedented 10-member ensemble using a high-resolution Earth system model that successfully captures observed cooling. This improvement is driven by more realistic ocean dynamics, in which explicitly resolved eddies regulate ocean-atmosphere feedbacks which amplifies ozone-induced cooling.

Main Text

Introduction

The Southern Ocean in the past few decades has been characterized by strengthening zonal surface winds (τ_x) and associated meridional sea level pressure (SLP) gradients, decreasing sea surface temperature (SST), and expanding sea-ice cover. Rapid stratospheric ozone depletion over the South Pole since the 1970s is hypothesized to drive these surface signals by cooling the lower polar stratosphere, which in turn alters vertical wave propagation and wave-mean flow interactions in the troposphere, resulting in a strengthening and poleward shift of the westerlies, including at the surface over the Southern Ocean (1-6).

This hypothesis has been partially validated through observations and numerical experiments (2, 6-11), but Southern Ocean trends remain systematically under-represented in Earth system models participating in both phases 5 and 6 of the Coupled Model Intercomparison Project (CMIP5 and CMIP6) (12-14). Although coarse-/low-resolution (nominal ~1°, or ~100 km, ocean and atmosphere) CMIP models fail to capture the observed SST cooling trends, simulations with fixed pre-depletion ozone concentrations have been found to produce warmer SST trends than simulations with realistic ozone depletion (9).

Until recently, the Southern Ocean cooling has largely been considered to be externally forced rather than internally generated. However, given the inability of climate models to reproduce these SST trends, the complete picture remains unexplained. Indeed, a study of observed climate trends over the pre-ozone depletion period (1950-1978) and the ozone-depletion period (1979-2011) found pronounced multidecadal variability of similar magnitude in both time periods (15). Furthermore, a comparison of long-term variability in Antarctic sea-ice extent with the Southern Annular Mode (SAM) and ozone trends in observations and CMIP5 models suggests that atmosphere-forced variability only explains a small fraction of the Antarctic sea-ice trends during the last four decades (16). Similar conclusions are obtained for the ozone-driven component of the Southern Ocean SST cooling (8).

The role of the oceanic response to ozone-driven surface trends and its potential influence on SST, SLP, and τ_x has yet to be adequately investigated and is a focus of this study. Observation-based analysis and ocean model output show that wind-driven upwelling in the Southern Ocean can impact the SST around Antarctica by vertical and northward transport of cooler deep waters (17). Furthermore, surface buoyancy fluxes (and thus the above surface trends) estimated from observations and computed from coupled model output are highly sensitive to the net ocean circulation changes in response to wind stress changes (18). A recent study using CMIP5 simulations, along with additional multi-resolution, fixed CO_2, and future scenario (Representative Concentration Pathway 8.5, RCP8.5) coupled experiments concluded that eddy-resolving Earth system models simulate a more realistic ocean circulation, which enhances equatorward ocean heat transport (Q) under strengthened westerlies and more efficiently cools the ocean around Antarctica, thereby delaying sea-ice decline seen in low-resolution CMIP5 simulations (19). Consistent with these findings, a more recent study comparing high-resolution (nominal ~0.1° in ocean and sea-ice and nominal ~0.25° in atmosphere and land) and low-resolution (nominal ~1° in all components) decadal prediction systems showed improved representation of the Southern Ocean cooling trend in the high-resolution system, leading to better global prediction skill and signal-to-noise characteristics (20). The enhanced equatorward ocean heat transport in the high-resolution system is hypothesized to play a key role in this improvement. Motivated by these studies, the present work further investigates the role of ocean eddy compensation in the Southern Ocean cooling trend.

The dependence of simulated ocean circulation on horizontal resolution arises from an ocean model's ability to explicitly represent mesoscale eddies (with length scales of ~10-100 km) and their energetic and thermodynamic effects on large-scale circulation. Coarse-resolution (nominal ~1°) ocean models cannot resolve these eddies, so their effects must be parameterized. Changes in wind-driven upwelling in the Southern Ocean are theorized to be partially or fully compensated by eddy-induced circulations (21-23), a concept confirmed in idealized numerical simulations (24, 25). While some global ocean and Earth system models capture this "eddy compensation" (26-31), many models and data-synthesis products simulate weak or more complex eddy compensation (28, 32-38), indicating that representing a realistic balance between wind-driven and eddy-induced circulations remains subject to considerable uncertainty.

In this study, we expand upon how model horizontal resolution impacts capturing or representations of the observed SST, SLP, and τ_x trends during 1980-2022 at the Southern Ocean latitudes, by considering two 10-member historical ensembles of the Community Earth System Model (CESM).Specifically, one ensemble was conducted at high-resolution (CESM-HR; nominal ~0.1° ocean and sea-ice and ~0.25° atmosphere and land) and the other at low-resolution (CESM-LR; nominal ~1° for all component models) (39-41). The ensemble approach allows us to account for internal variability. To isolate the individual impacts of atmospheric and oceanic model

resolution, we also analyze atmosphere-only simulations following the Atmosphere Model Intercomparison Project (AMIP) protocol and forced ocean—sea-ice (FOSI) simulations following the Ocean Model Intercomparison Project (OMIP) (42) protocol. We note that additional mechanisms of Southern Ocean SST cooling have been proposed, such as surface freshening associated with ice sheet melt, which increases stratification and reduces the vertical flux of heat from the pycnocline (43-46); however, these mechanisms are not the focus of this study.

Observation-based and Simulated Trends

Observation-based trends in SST, SLP, and τ_x over the period 1980-2022 are more realistically captured by CESM-HR compared to its low-resolution counterpart (CESM-LR): Fig. 1. Specifically, the ensemble-mean SST trend in CESM-HR (Fig. 1F) exhibits a cooling trend in the South Pacific (120°E-60°W, south of 50°S) region where the strongest cooling is seen in observations (Fig. 1B). Multiple CESM-HR ensemble members simulate cooling trends across the Southern Ocean (south of 50°S), see SI Appendix Fig. S1, and the regional averages in the South Pacific of those members are comparable to those of observations (Figs. 1A and 1E), suggesting that both external forcing (given by the ensemble-mean) and internal variability (given by the ensemble-spread) contribute. As for the low-resolution simulation, the CESM-LR ensemble does not show cooling trends either in the ensemble mean or individual ensemble members (Fig. 1I, Fig. 1J, and SI Appendix Fig. S2), except for one CESM-LR member which shows a slight negative trend. The Southern Ocean warming in CESM-LR resembles the 40-member CESM1 Large Ensemble (CESM1-LE) (47), which is based on a different low-resolution configuration of CESM1 which participated in CMIP5, shown in Figs. 1I and SI Appendix Fig. S5B for comparison. The CESM-HR ensemble-mean also captures the cooling trend in the Southeastern Tropical Pacific (Fig. 1F), a feature many other high-resolution models struggle to reproduce (48). The origin of this feature and its potential connection to the Southern Ocean cooling trend (49, 50) will be addressed in future work.

Attribution of Southern Ocean Atmospheric Trends

Both CESM-HR and CESM-LR are driven by the same external radiative forcings. However, CESM-LR shows much weaker trends in τ_x and SLP compared to CESM-HR (Figs. 1D, 1H, 1L and 1C, 1G, 1K), indicating that the simulated response is resolution-dependent and/or that 10 ensemble members are not sufficient to isolate the forced response. One possibility is that the high-resolution atmosphere in CESM-HR produces a stronger response to ozone forcing, which could drive stronger SST cooling. To test this hypothesis, we analyzed AMIP simulations in which both the high- and low-resolution atmosphere models are forced with the same ~0.25° resolution observed SST forcing dataset from the CMIP6 HighResMIP protocol (51) from 1950 to 2014. The historical radiative forcings are identical to those used in CESM-HR and CESM-LR. There are 3 ensemble members for the high-resolution simulations (AMIP-HR) and 10 ensemble members for the low-resolution (AMIP-LR). To ensure a fair comparison with AMIP-HR, we randomly selected 3 of the 10 AMIP-LR ensemble members and used bootstrap resampling with replacement to assess the sampling uncertainty associated with 3-member averages. The results show that over 1980-2014 AMIP-HR and AMIP-LR produce similar trends in τ_x and SLP, particularly in the Southern Ocean regions where the trends show τ_x strengthening and SLP meridional gradient intensification of similar spatial structure and magnitude to those in ERA5. (Fig. 2). This suggests that the improved trend simulation in CESM-HR is not primarily due to higher atmospheric resolution, since

AMIP-LR can reproduce the observed Southern Ocean surface trends when forced by the same SST forcing and radiative forcings. Rather, differences in SST trends between CESM-HR and CESM-LR may be responsible for the differently simulated surface trends, which are affected by ocean model resolution. Consequently, we next examine the impact of ocean model resolution using simulations forced with the same atmospheric conditions.

Ocean Processes Contributing to the Cooling Trend

We compared two sets of FOSI simulations driven by the same atmospheric forcing based on the JRA-55 reanalysis (52): one using the ocean and sea-ice components of CESM-HR (FOSI-HR) (20) and the other using those of CESM-LR (FOSI-LR). These FOSI simulations were run for four repeat cycles of the JRA-55-based forcing over 1958-2018, where the final time-step of each cycle is used as the initial condition of the next cycle. We utilize cycles 2-4 as a 3-member ensemble for each, excluding the first cycle due to ocean model spin-up. Because the FOSI simulations are constrained by the observation-based surface air temperature, which contains the cooling trend, the simulated SSTs may not provide a reliable metric for assessing model skill. Therefore, to better evaluate the ocean cooling away from the constrained surface layers, we instead use the simulated subsurface temperatures averaged from 100 to 500 m as a measure of the cooling trend. In Fig. 3, we plot the linear trends in subsurface temperatures as simulated in FOSI-HR and FOSI-LR, with a comparison to the Global Ocean Physics Reanalysis (GLORYS) (53) as an observation-based dataset. The results indicate a stronger high latitude upper ocean cooling trend in FOSI-HR compared to FOSI-LR, in better agreement with GLORYS. This result supports that of (20), where the same FOSI-HR simulation reveals positive sea-ice extent trends in better agreement with recent observations than its low-resolution counterpart (see their Supp. Fig. 15).

Since the cooling signal penetrates throughout the subsurface, its vertical structure is of interest. The cooling signal is found across all sectors of the Southern Ocean in observations at the surface (Fig. 1B) and at depth in the GLORYS reanalysis (Fig. 3A) and FOSI-HR (Fig. 3B), with peak cooling found in the South Pacific sector in both cases. We focus on the South Pacific profile by extracting a vertical slice and zonally averaging ocean temperatures across 160°W-145°W where the front is strong and oriented in the zonal direction. We find that the deep cooling near 55°S and extending to 1300 m in FOSI-HR is aligned with steeply sloped isotherms in the climatology, consistent with GLORYS and in contrast to the flatter climatological isotherm slopes in FOSI-LR (Figs. 3D-F). In line with this difference in stratification, FOSI-LR transports on average about twice as much heat poleward across 50°S compared to FOSI-HR, delivering more heat to the Southern Ocean high latitudes ($\mathrm{Q}_{\mathrm{total}}$ in Figs. 4A-B). We used 50°S since it corresponds to the latitude of peak meridional SST gradient in observations (Fig. 1B) as well as peak upper ocean temperature gradient in GLORYS (Figs. 3A and 3C). Here we define $\mathrm{Q}_{\mathrm{total}}$ as the time-mean of the vertically and zonally integrated product of the instantaneous ocean meridional velocity (v) and the ocean temperature (T). Additionally, the $\mathrm{Q}_{\mathrm{total}}$ trend across 50°S is poleward in FOSI-LR but equatorward in FOSI-HR, suggesting an increasing ocean heat supply to the Southern Ocean in FOSI-LR but a decreasing supply in FOSI-HR (Figs. 4C-D). This result corroborates the findings of (20) who analyzed the same JRA-55-forced FOSI-HR simulation but compared it to a different FOSI-LR simulation that used a different atmospheric forcing dataset (see (54) for those forcing details). Here, we replicate the ocean heat transport analysis from that study to clarify whether resolution related differences in ocean heat transport are robust when the ocean is subject to the same atmospheric forcing. A similar trend of decreasing heat supply to the Southern Ocean is also found in a different high-resolution ocean model (55).

We decompose Q_{total} into its Eulerian-mean component, Q_{mean}, computed from the monthly-averaged v and T, and its transient component, Q_{eddy}, computed as the difference between Q_{total} and Q_{mean}. Q_{mean} is associated with large-scale ocean circulation driven by atmospheric forcing, and Q_{eddy} is associated with mesoscale eddies driven by internal ocean dynamics. This decomposition reveals that Q_{mean} has similar magnitudes across 50°S in FOSI-LR and FOSI-HR. This indicates that the same atmospheric forcing generates comparable large-scale circulation-driven Q_{mean} regardless of ocean model resolution. In contrast, Q_{eddy} differs significantly between FOSI-HR and FOSI-LR, with FOSI-HR showing much weaker eddy heat transport and a weaker trend. This difference arises from how eddy-induced transports are computed: CESM-HR resolves eddies explicitly, while CESM-LR uses the Gent–McWilliams (GM) parameterization (56). The GM scheme is based on the classical baroclinic instability theory, which expects compensation between Q_{mean} and Q_{eddy}. This compensation is evident in FOSI-LR (Fig. 4A) but surprisingly is mostly absent in FOSI-HR (Fig. 4B), even when the atmospheric forcing is the same, thus putting the findings of (20) on firmer footing. Given that FOSI-HR and CESM-HR (and FOSI-LR and CESM-LR) use the same ocean component, we explicitly hypothesize that this difference in eddy compensation between FOSI-HR and FOSI-LR contributes to the stronger SST cooling trend found in the fully coupled CESM-HR compared to that of CESM-LR.

A similar decomposition of the meridional overturning circulation (MOC) streamfunction based on integrating meridional velocity vertically and zonally over isopyncal layers following (25, 32), $\Psi_{total} = \Psi_{mean} + \Psi_{eddy}$, reveals an analogous contrast between FOSI-LR and FOSI-HR (SI Appendix Fig. S3). In both simulations, the wind-driven Eulerian-mean streamfunction is characterized by a clockwise overturning cell centered at 50°S with equatorward transport near the surface. The anti-clockwise eddy-driven overturning, which results in poleward transport near the surface that slumps the isotherms (or isopycnals), has a stronger time-mean and a stronger trend in FOSI-LR, resulting in a weaker residual overturning. Meanwhile, FOSI-HR simulates weaker transient eddy and stronger residual clockwise overturning cells, which contributes to stronger upwelling and equatorward transport of cold polar waters.

Ocean Responses in CESM-HR Contributing to the Cooling Trend

The above discussion has established that the ocean components of CESM-HR and CESM-LR respond to the observed atmospheric forcing trends differently due to their different representations of ocean eddies. The differing ocean response in Q and MOC simulated in FOSI-HR and FOSI-LR, which is likely responsible for the increased cooling trend, may also be at play in the trends simulated by CESM-HR and CESM-LR under historical radiative forcing, although the differing magnitudes of simulated zonal wind stress trends may complicate its detection. We have 10 high-resolution realizations of the ocean response to the same radiative forcing. There is a substantial spread in the Southern Ocean SST trends (1980-2022) across the ensemble members, ranging from -0.8 to +0.8 °C (Fig. 1E and SI Appendix Fig. S1). Focusing on the South Pacific region (150°E-60°W, south of 50°S) where the observed cooling is the strongest, we classify CESM-HR ensemble members by their SST trends averaged in this region. By comparing the average of the 3 members with cooling (blue circles in Fig. 1E) and the average of the 3 members with the strongest warming (red circles in Fig. 1E), we find the two groups differ in their SST, SLP, and τ_x trends (Fig. 5). The cool group (Figs. 5A-C) exhibits trends similar to observations in both pattern and magnitude (Figs. 1B-D), while the warm group (Figs. 5D-F) shows muted cooling in the polar regions and exacerbated warming at lower latitudes, along with substantially weaker SLP and τ_x trends.

This contrast of SST trends is consistent with the difference between the linear trends of Q_{total} and Ψ_{total} for the same grouping of ensemble members as shown in Fig. 6. Compared to the warm group, the cool group simulates about twice the magnitude of total northward heat transport trends at 50°S, as well as positive Q_{total} trends in the 70°S to 60°S latitude band (Figs. 6A and 6B). Similarly, the linear trends of residual overturning circulation in the cool group indicate enhanced strengthening of the clockwise overturning cell, resulting in more upwelling and northward transport compared to the warm group. Similar analysis of the Eulerian-mean and transient eddy overturning reveals a stronger positive trend of both the Eulerian-mean and transient eddy streamfunctions in the cool group compared to the warm group (SI Appendix Fig. S4). These findings point to the representation and amount of eddy compensation in the Southern Ocean as a key factor for accurately simulating the cooling trend in Earth system models. It should be noted that our analysis pertains primarily to the internally generated component of the Southern Ocean SST trends (1980-2022) in CESM-HR rather than the forced response to ozone depletion and other radiative forcing agents.

Discussion

While previous work emphasizes the role of stratospheric ozone depletion in the high-latitude Southern Hemisphere in driving the observed Southern Ocean SST cooling trend over the past four decades (2, 9), this study highlights the potential role of ocean dynamics, in particular eddy heat transport, in regulating wind-driven atmosphere-ocean feedback sustaining and amplifying the ozone-driven trend. CESM-HR simulates trends of SST, SLP, and τ_x in better agreement with observation-based data compared to CESM-LR. These improvements cannot be attributed to atmospheric model resolution, since AMIP-LR and AMIP-HR simulate similar SLP and τ_x trends under identical SST and radiative forcing. The results of FOSI-LR and FOSI-HR subject to the same observation-based atmospheric forcing show that the Southern Ocean cooling trends are stronger and penetrate deeper in FOSI-HR compared to FOSI-LR. Analysis of the ocean meridional heat transport and meridional overturning circulation reveals that the differences lie in the simulated ocean response to atmospheric forcing at low and high resolution. The difference in residual heat transport and overturning circulation trends is due to differences in the transient eddy response, which is parameterized in FOSI-LR but explicitly represented in FOSI-HR. FOSI-LR overcompensates the wind-driven transport with its parameterized transient eddy transport, leading to an overall increase in southward heat transport and a relative warming in the Southern Ocean. Meanwhile, the weaker transient eddy transport in FOSI-HR allows the wind-driven overturning cell to more efficiently upwell colder waters, reducing southward heat transport into Southern Ocean. These results contrast with the theoretical concept of “eddy compensation”, whereby changes in the Eulerian-mean overturning are compensated by transient eddies. Comparison of Southern Ocean SST trends can be made with other high-resolution models from the High-Resolution Model Intercomparison Project (HighResMIP) (51) which do indeed show some cooling (SI Appendix Fig. S5A), but since the majority of the models contributing to HighResMIP utilize a mix of both permitted and parameterized transient eddy heat transport, a clean comparison to FOSI-HR or CESM-HR (where no eddy parameterization is used) cannot be made.

Another key finding is the substantial spread in simulated trends across CESM-HR ensemble members, reinforcing that the cooling trend is not a simple response to ozone depletion but is strongly influenced by internal coupled system dynamics. Analysis of individual ensemble members reveals that those with a stronger wind-driven response exhibit enhanced overturning and larger equatorward heat transport trends, leading to stronger cooling. Despite identical ozone

forcing and comparable transient eddy responses, the wind stress trends are also stronger in the cool members than in the warm members. If Southern Ocean surface trends were purely ozone-driven, all ensemble members would be expected to show similar behavior. Instead, clear differences emerge between simulated surface wind trends between the warm and cool groups when examined over three overlapping 26-year windows spanning 1980 to 2015, with the cool groups resembling observation-based surface wind trends from ERA5 more than the warm groups (Fig. 7). During the first window, 1980 to 2005, both observation-based trends (ERA5 and ERSSTv5) and the two CESM-HR groups show an initial phase of comparable westerly intensification and modest SST cooling, most likely driven by the strong ozone depletion trend during the 1970 to 2000 period (SI Appendix Fig. S6). After this initial phase, the cool group simulates progressively stronger wind stress trends accompanied by intensified SST cooling through the 1985 to 2010 and 1990 to 2015 windows (Figs. 7G-L), in line with trends seen in ERA5 and ERSSTv5 (Figs. 7A-F), while the warm group simulates relative static trends (Figs. 7M-R). The fact that both the SST and τ_x trends in the observation and the cool group strengthen in tandem and persist after the main ozone depletion period suggests the emergence of a coupled atmosphere-ocean feedback. In contrast, both SST and wind stress trends weaken in the warm group, resulting in minimal SST cooling and only weak wind stress trends by the final window. Finally, the lack of perfect spatial coincidence between peak SST cooling and peak zonal surface wind stress strengthening indicates the combined influence of wind driven ocean cooling and atmospheric responses to evolving SST anomalies (Fig. 7). Also apparent is zonal asymmetry of the wind stress trend spatial patterns in both observation and the two groups through the latter three windows, manifesting in the eastern South Pacific. A purely ozone-driven wind stress response should be zonally uniform, suggesting other factors may be amplifying the wind stress response specifically in the Pacific sector. This zonal asymmetry in the wind stress trends also resembles the Interdecadal Pacific Oscillation Rossby wave-train pattern (57); this potential teleconnection and its influence on wind stress and SST trends will be addressed in future work.

Further analysis is required to identify the coupling mechanisms responsible for the divergence among ensemble members of CESM-HR. However, a substantial body of theoretical and modeling studies provides a physical basis for linking Southern Ocean surface wind responses to underlying SST anomalies (58-62). These studies point to two well established mechanisms operating within the atmospheric boundary layer. The first involves modulation of vertical turbulent stress divergence by SSTs, commonly referred to as the vertical mixing mechanism (61, 63-69) The second involves adjustment of atmospheric boundary layer pressure to SST fronts, often described as the pressure adjustment mechanism (70-72). In addition to these boundary layer processes, SST variability may also influence surface winds through changes in atmospheric baroclinic eddy flux convergence, which extends beyond the boundary layer. Idealized atmospheric general circulation model experiments demonstrate that sharp SST gradients are critical in translating ozone-induced stratospheric changes to the surface (73). They can also help maintain near surface baroclinicity, leading to enhanced eddy growth rates and increased eddy momentum flux convergence, which can maintain or even strengthen eddy driven westerly jets (74, 75), highlighting the potential for SST trends to exert an amplifying influence on surface wind responses.

By combining the arguments of (2, 9) with our own results and the above discussion, we hypothesize that ozone-driven intensification of the Southern Ocean westerlies in the late 20th century enhances equatorward Ekman transport, leading to surface ocean cooling in the Southern Ocean. This cooling strengthens the meridional SST gradient, which in turn feeds back onto the atmosphere by strengthening the meridional sea-level pressure gradient, further intensifying the westerlies and reinforcing the cooling trend through a positive feedback loop. Although a detailed

analysis of this coupled feedback is beyond the scope of this study and will be presented in future work, we identify a positive trend in the meridional SST gradient that coincides with trends in the meridional sea-level pressure gradient and zonal wind stress in both ERA5 and CESM-HR, but not in CESM-LR (SI Appendix Fig. S7). The effectiveness of this feedback depends on the degree of ocean eddy compensation, which opposes the wind-driven component of the meridional overturning circulation. Unlike CESM-LR and other standard low-resolution Earth system models that rely on parameterized eddy heat transport, the eddy-rich CESM-HR exhibits weaker eddy compensation. This allows the Ekman feedback to operate more effectively, resulting in a stronger Southern Ocean cooling trend that aligns more closely with observations.

If the development of the ozone hole initiated Southern Ocean SST cooling in recent decades, then recovery of stratospheric ozone combined with increasing of other greenhouse gases projected over the 21st century should lead to a cessation of cooling in the coming decades. Utilizing the RCP8.5 projection portion of the CESM-HR, we examine the evolution of the simulated ensemble-mean SST trends over the 1980-2100 period by computing the linear trends in four 46-year windows that cover the whole time-series. As seen in SI Appendix Fig. S8, the first interval, 1980-2025, resembles the linear trend shown in Fig. 1, excepting the Southeastern Tropical Pacific cooling signal which has already ceased. Through the following two periods, 2005-2050 and 2030-2075, the Southern Ocean cooling trend diminishes, and by the final interval, 2055-2100, warming dominates both the Tropical Pacific and the Southern Ocean. This transition highlights the key role ozone trends play in recent Southern Ocean cooling, in line with the arguments of (2). The hypothesized Ekman feedback that strengthens the Southern Ocean cooling in CESM-HR requires an initial ozone-depletion-forced surface cooling. As Antarctic ozone stabilizes in the early 21st century (SI Appendix Fig. S6) and the ozone hole begins to close, the associated upper-level pressure gradients weaken, effectively shutting down the Ekman feedback, and projected greenhouse gas increase suppresses the Southern Ocean cooling. Future work is planned to validate the proposed dynamical processes, the dependence of global trends on Antarctic ozone trends, and connections between the high latitude Southern Hemisphere and the tropics within the CESM-HR framework, specifically by comparing the role of ocean-atmosphere interactions as simulated in CESM-LR and CESM-HR.

Materials and Methods

Datasets. The observed sea surface temperature data shown in Fig. 1 were obtained from the Extended Reconstructed Sea Surface Temperature Version 5 (ERSSTv5) (76) provided by the NOAA National Centers for Environmental Information from their website at https://psl.noaa.gov/data/gridded/data.noaa.ersst.v5.html (77).

The zonal wind and sea level pressure data shown in Fig. 1 were obtained from the ERA5 (78) which can be found at https://cds.climate.copernicus.eu/datasets/reanalysis-era5-single-levels-monthly-means?tab=overview (79).

The precipitation data used in Fig. 2C were obtained from the Global Precipitation Climatology Project (GDCP) Climate Data Record (CDR), Version 2.3 (Monthly) (80), available at https://www.ncei.noaa.gov/access/metadata/landing-page/bin/iso?id=gov.noaa.ncdc:C00979 (81).

The ocean reanalysis data shown in Fig. 2 are from the Global Ocean Physics Reanalysis 12 Version 1 (GLORYS12V1) (53), an E.U. Copernicus Marine Service data product, available at https://data.marine.copernicus.eu/product/GLOBAL_MULTIYEAR_PHY_001_030/services (82).

The CESM-LR and CESM-HR simulations used in this study were performed primarily under the NSF-funded MESACLIP Project (Understanding the Role of Mesoscale Atmosphere-Ocean Interactions in Seasonal-to-Decadal Climate Prediction) (39, 41) https://project.cgd.ucar.edu/projects/MESACLIP/index.html). This project is a collaboration between Texas A&M University and National Science Foundation (NSF) National Center for Atmospheric Research (NCAR). The CESM-HR and CESM-LR datasets are publicly available through the NSF NCAR Geoscience Data Exchange (GDEX) platform at https://gdex.ucar.edu/datasets/d651029/ (CESM-HR pre-industrial control) (83), https://gdex.ucar.edu/datasets/d651007/ (CESM-HR historical ensemble) (84), https://gdex.ucar.edu/datasets/d651009/ (CESM-HR RCP 8.5 future ensemble) (85), and https://gdex.ucar.edu/datasets/d651030/ (CESM-LR) (86). Surface fields of CESM output plotted in all figures were re-gridded to standard 1°x1° grids. The associated AMIP and FOSI simulations utilize the same atmosphere and ocean—sea-ice components.

Five members of the High-Resolution Model Intercomparison Project (HighResMIP) (51) were used as a comparison to CESM-HR Southern Ocean SST trends in SI Appendix Fig. S5A. Models used from HighResMIP are CESM-HRMIP (87-89), CCMC-CM2-VHR4 (90, 91), the 3-member EC-Earth3P-HR (92, 93), HadGEM3-GC31-HH (94, 95), and MPI-ESM1-2-XR (96, 97), for a total of 7 realizations in the multi-model-mean. The HighResMIP datasets can be found at https://esgf-node.llnl.gov/projects/cmip6/ (98). Similarly, the CESM Large Ensemble (CESM1-LE) (47) was used as a comparison to CESM-LR Southern Ocean SST trends in Fig. 1I and SI Appendix Fig. S5B; the CESM1-LE dataset can be found on the NSF NCAR GDEX platform at https://gdex.ucar.edu/datasets/d651027/ (99).

For the regional average of Southern Ocean SST linear trend shown in Fig. 1A, SST data from two other observational/reanalysis data products were used for comparison to ERSSTv5: ERA5 and the U.K. Met Office Hadley Centre Sea Ice and Sea Surface Temperature data set (HadISST) (100). HadISST data can be found at https://www.metoffice.gov.uk/hadobs/hadisst/data/download.html or on the NDF NCAR GDEX platform at https://gdex.ucar.edu/datasets/d277003/ (101).

Linear Trends. For all linear trends in observation-based data or model output, the annual-mean data were used, and a linear regression was applied to extract the trends. Additionally, for the linear trends calculated for CESM-HR, CESM-LR, HighResMIP, and CESM1-LE, the underlying drift in the respective Pre-Industrial Control (PI-cntl) period was removed.

Meridional Heat Transport and Overturning Circulation Decomposition. For the simulated oceanic meridional heat and volume transports, the following residual-mean decomposition is made: $\mathrm{u}_{\mathrm{total}} = \bar{\mathrm{u}} + \mathrm{u}'$, where $\bar{\mathrm{u}}$ and u' are the time-mean and anomaly of some variable u, and $\mathrm{u}_{\mathrm{total}}$ is the total (or residual).
For the meridional heat transport (Q) shown in Figs. 4 and 6, the decomposition is computed by the following operation:

$$Q_{total} = Q_{mean} + Q_{eddy} = \overline{\oint \int_{-H}^{0} vT \, dz \, dx} = \oint \int_{-H}^{0} \bar{v}\bar{T} dz \, dx + \overline{\oint \int_{-H}^{0} v'T' dz \, dx}$$

Where v is the ocean meridional velocity, T is the ocean temperature, H is the ocean depth at any gridpoint, and the integrals are applied from ocean bottom to the surface and then zonally.

For the overturning circulation (Ψ) shown in Fig. 6 and Supp. Figs. 2 and 3, the decomposition in density space (σ) is calculated following:

$$\Psi_{total} = \Psi_{mean} + \Psi_{eddy} = \overline{\oint \int_{\sigma}^{\sigma_s} vh \, d\sigma dx} = \oint \int_{\bar{\sigma}}^{\overline{\sigma_s}} \bar{v}\bar{h} \, d\sigma dx + \overline{\oint \int_{\sigma}^{\sigma_s} v'h' d\sigma dx}$$

Where σ is an isopycnal layer, σ_s is the surface density, h is the thickness of an isopycnal layer, and the integrals are applied from a maximum isopycnal σ at depth to the surface density σ_s and then zonally. In this study, we utilize the density referenced to the 2000 m depth (σ_2).

Acknowledgments

The ensemble of the historical and future simulations analyzed in this study was initially supported by the International Laboratory for High-Resolution Earth System Prediction (iHESP) and subsequently by the MESACLIP project (Understanding the Role of MESoscale Atmosphere-Ocean Interactions in Seasonal-to-Decadal CLImate Prediction), funded by the US National Science Foundation (NSF) grant AGS-2231237 and additional support from the Gulf Research Program of the U.S. National Academies of Sciences, Engineering, and Medicine (2000013283); the Department of Commerce through NOAA OAR's Climate Variability and Predictability Program (NA24OARX431G0047); and The Nature Conservancy. Nine ensemble members were performed on Frontera at the Texas Advanced Computing Center (TACC; http://www.tacc.utexas.edu) at the University of Texas at Austin and Derecho (https://doi.org/10.5065/ qx9a-pg09) at the Computational and Information Systems Laboratory (CISL) of the NSF National Center for Atmospheric Research (NCAR). We also acknowledge computing resources provided by the Texas A&M High Performance Computing (https://hprc.tamu.edu). The pre-industrial simulation and the first ensemble member of the historical and future simulations were completed under iHESP. We extend special thanks to Jim Edwards for assistance in porting and optimizing the CESM1.3 code. NSF NCAR is a major facility sponsored by the US NSF under cooperative agreement number 1852977. T.R.P. and P.C. were partially supported by a collaboration grant between Texas A&M University and Los Alamos National Laboratory. We thank Wilbert Weijer for this collaboration.

References

1. W. Cai, Antarctic ozone depletion causes an intensification of the Southern Ocean super-gyre circulation - art. no. L03712. *Geophys Res Lett* **33** (2006).
2. D. L. Hartmann, The Antarctic ozone hole and the pattern effect on climate sensitivity. *P Natl Acad Sci USA* **119** (2022).
3. L. M. Polvani, D. W. Waugh, G. J. P. Correa, S. W. Son, Stratospheric Ozone Depletion: The Main Driver of Twentieth-Century Atmospheric Circulation Changes in the Southern Hemisphere. *J Climate* **24**, 795-812 (2011).
4. D. W. J. Thompson, S. Solomon, Interpretation of recent Southern Hemisphere climate change. *Science* **296**, 895-899 (2002).
5. D. W. J. Thompson *et al.*, Signatures of the Antarctic ozone hole in Southern Hemisphere surface climate change. *Nat Geosci* **4**, 741-749 (2011).
6. X. Y. Yang, R. X. Huang, D. X. Wang, Decadal changes of wind stress over the Southern Ocean associated with Antarctic ozone depletion. *J Climate* **20**, 3395-3410 (2007).

7. A. Banerjee, J. C. Fyfe, L. M. Polvani, D. Waugh, K.-L. Chang, A pause in Southern Hemisphere circulation trends due to the Montreal Protocol. *Nature* **579**, 544-548 (2020).
8. Y. Dong, L. M. Polvani, D. B. Bonan, Recent Multi-Decadal Southern Ocean Surface Cooling Unlikely Caused by Southern Annular Mode Trends. *Geophys Res Lett* **50** (2023).
9. Y. Dong, L. M. Polvani, Y. T. Hwang, M. R. England, Stratospheric ozone depletion has contributed to the recent tropical La Niña-like cooling pattern. *Npj Clim Atmos Sci* **8** (2025).
10. S. Haase, J. Fricke, T. Kruschke, S. Wahl, K. Matthes, Sensitivity of the Southern Hemisphere circumpolar jet response to Antarctic ozone depletion: prescribed versus interactive chemistry. *Atmos Chem Phys* **20**, 14043-14061 (2020).
11. L. E. Revell, F. Robertson, H. Douglas, O. Morgenstern, D. Frame, Influence of Ozone Forcing on 21st Century Southern Hemisphere Surface Westerlies in CMIP6 Models. *Geophys Res Lett* **49** (2022).
12. K. C. Armour *et al.*, Sea-surface temperature pattern effects have slowed global warming and biased warming-based constraints on climate sensitivity. *Proceedings of the National Academy of Sciences* **121**, e2312093121 (2024).
13. Y. H. Hu, W. S. Tian, Y. X. Dong, J. K. Zhang, Evaluating the Seasonal Responses of Southern Ocean Sea Surface Temperature to Southern Annular Mode in CMIP6 Models. *Geophys Res Lett* **51** (2024).
14. R. C. J. Wills, Y. Dong, C. Proistosecu, K. C. Armour, D. S. Battisti, Systematic Climate Model Biases in the Large-Scale Patterns of Recent Sea-Surface Temperature and Sea-Level Pressure Change. *Geophys Res Lett* **49** (2022).
15. T. T. Fan, C. Deser, D. P. Schneider, Recent Antarctic sea ice trends in the context of Southern Ocean surface climate variations since 1950. *Geophys Res Lett* **41**, 2419-2426 (2014).
16. L. M. Polvani *et al.*, Interannual SAM Modulation of Antarctic Sea Ice Extent Does Not Account for Its Long-Term Trends, Pointing to a Limited Role for Ozone Depletion. *Geophys Res Lett* **48** (2021).
17. K. C. Armour, J. Marshall, J. R. Scott, A. Donohoe, E. R. Newsom, Southern Ocean warming delayed by circumpolar upwelling and equatorward transport. *Nat Geosci* **9**, 549-+ (2016).
18. H. D. Chen, A. K. Morrison, C. O. Dufour, J. L. Sarmiento, Deciphering Patterns and Drivers of Heat and Carbon Storage in the Southern Ocean. *Geophys Res Lett* **46**, 3359-3367 (2019).
19. T. Rackow *et al.*, Delayed Antarctic sea-ice decline in high-resolution climate change simulations. *Nat Commun* **13** (2022).
20. S. G. Yeager *et al.*, Reduced Southern Ocean warming enhances global skill and signal-to-noise in an eddy-resolving decadal prediction system. *Npj Clim Atmos Sci* **6** (2023).
21. J. Marshall, T. Radko, Residual-mean solutions for the Antarctic Circumpolar Current and its associated overturning circulation. *Journal of Physical Oceanography* **33**, 2341-2354 (2003).
22. J. Marshall, T. Radko, A model of the upper branch of the meridional overturning of the southern ocean. *Prog Oceanogr* **70**, 331-345 (2006).
23. M. P. Meredith, A. C. N. Garabato, A. M. Hogg, R. Farneti, Sensitivity of the Overturning Circulation in the Southern Ocean to Decadal Changes in Wind Forcing. *J Climate* **25**, 99-110 (2012).
24. R. Abernathey, J. Marshall, D. Ferreira, The Dependence of Southern Ocean Meridional Overturning on Wind Stress. *Journal of Physical Oceanography* **41**, 2261-2278 (2011).
25. J. Marshall, K. Speer, Closure of the meridional overturning circulation through Southern Ocean upwelling. *Nat Geosci* **5**, 171-180 (2012).
26. R. Farneti, T. L. Delworth, The Role of Mesoscale Eddies in the Remote Oceanic Response to Altered Southern Hemisphere Winds. *Journal of Physical Oceanography* **40**, 2348-2354 (2010).

27. R. Farneti, T. L. Delworth, A. J. Rosati, S. M. Griffies, F. R. Zeng, The Role of Mesoscale Eddies in the Rectification of the Southern Ocean Response to Climate Change. *Journal of Physical Oceanography* **40**, 1539-1557 (2010).
28. R. Farneti *et al.*, An assessment of Antarctic Circumpolar Current and Southern Ocean meridional overturning circulation during 1958-2007 in a suite of interannual CORE-II simulations. *Ocean Modelling* **93**, 84-120 (2015).
29. P. R. Gent, G. Danabasoglu, Response to Increasing Southern Hemisphere Winds in CCSM4. *J Climate* **24**, 4992-4998 (2011).
30. S. M. Griffies *et al.*, Impacts on Ocean Heat from Transient Mesoscale Eddies in a Hierarchy of Climate Models. *J Climate* **28**, 952-977 (2015).
31. A. K. Morrison, O. A. Saenko, A. M. Hogg, P. Spence, The role of vertical eddy flux in Southern Ocean heat uptake. *Geophys Res Lett* **40**, 5445-5450 (2013).
32. S. P. Bishop *et al.*, Southern Ocean Overturning Compensation in an Eddy-Resolving Climate Simulation. *Journal of Physical Oceanography* **46**, 1575-1592 (2016).
33. F. O. Bryan, P. R. Gent, R. Tomas, Can Southern Ocean Eddy Effects Be Parameterized in Climate Models? *J Climate* **27**, 411-425 (2014).
34. R. Farneti, P. R. Gent, The effects of the eddy-induced advection coefficient in a coarse-resolution coupled climate model. *Ocean Modelling* **39**, 135-145 (2011).
35. W. Liu, J. Lu, S. P. Xie, A. Fedorov, Southern Ocean Heat Uptake, Redistribution, and Storage in a Warming Climate: The Role of Meridional Overturning Circulation. *J Climate* **31**, 4727-4743 (2018).
36. P. Spence, O. A. Saenko, C. O. Dufour, J. Le Sommer, M. H. England, Mechanisms Maintaining Southern Ocean Meridional Heat Transport under Projected Wind Forcing. *Journal of Physical Oceanography* **42**, 1923-1931 (2012).
37. J. Viebahn, C. Eden, Towards the impact of eddies on the response of the Southern Ocean to climate change. *Ocean Modelling* **34**, 150-165 (2010).
38. D. L. Volkov, L. L. Fu, T. Lee, Mechanisms of the meridional heat transport in the Southern Ocean. *Ocean Dynam* **60**, 791-801 (2010).
39. P. Chang *et al.*, Future extreme precipitation amplified by intensified mesoscale moisture convergence. *Nat Geosci* 10.1038/s41561-025-01859-1 (2025).
40. P. Chang *et al.*, Uncertain future of sustainable fisheries environment in eastern boundary upwelling zones under climate change. *Commun Earth Environ* **4** (2023).
41. P. Chang *et al.*, An Unprecedented Set of High-Resolution Earth System Simulations for Understanding Multiscale Interactions in Climate Variability and Change. *J Adv Model Earth Sy* **12** (2020).
42. S. M. Griffies *et al.*, OMIP contribution to CMIP6: experimental and diagnostic protocol for the physical component of the Ocean Model Intercomparison Project. *Geosci Model Dev* **9**, 3231-3296 (2016).
43. C. de Lavergne, J. B. Palter, E. D. Galbraith, R. Bernardello, I. Marinov, Cessation of deep convection in the open Southern Ocean under anthropogenic climate change. *Nat Clim Change* **4**, 278-282 (2014).
44. Z. Kaufman, E. Wilson, A. Purich, R. Beadling, Y. C. Li, The Impact of Underestimated Southern Ocean Freshening on Simulated Historical Sea Surface Temperature Trends. *Geophys Res Lett* **52** (2025).
45. C. H. Kirkman, C. M. Bitz, The Effect of the Sea Ice Freshwater Flux on Southern Ocean Temperatures in CCSM3: Deep-Ocean Warming and Delayed Surface Warming. *J Climate* **24**, 2224-2237 (2011).
46. A. G. Pauling, C. M. Bitz, I. J. Smith, P. J. Langhorne, The Response of the Southern Ocean and Antarctic Sea Ice to Freshwater from Ice Shelves in an Earth System Model. *J Climate* **29**, 1655-1672 (2016).
47. J. E. Kay *et al.*, THE COMMUNITY EARTH SYSTEM MODEL (CESM) LARGE ENSEMBLE PROJECT A Community Resource for Studying Climate Change in the Presence of Internal Climate Variability. *B Am Meteorol Soc* **96**, 1333-1349 (2015).

48. S. Dhame, D. Olonscheck, M. Rugenstein, Higher-Resolution Climate Models Do Not Consistently Reproduce the Observed Tropical Pacific Warming Pattern. *J Climate* **38**, 3131-3149 (2025).
49. S. M. Kang *et al.*, Global impacts of recent Southern Ocean cooling. *P Natl Acad Sci USA* **120** (2023).
50. X. Y. Zhang, C. Deser, Tropical and Antarctic sea ice impacts of observed Southern Ocean warming and cooling trends since 1949. *Npj Clim Atmos Sci* **7** (2024).
51. R. J. Haarsma *et al.*, High Resolution Model Intercomparison Project (HighResMIP v1.0) for CMIP6. *Geosci Model Dev* **9**, 4185-4208 (2016).
52. H. Tsujino *et al.*, JRA-55 based surface dataset for driving ocean-sea-ice models (JRA55-do). *Ocean Modelling* **130**, 79-139 (2018).
53. J.-M. Lellouche *et al.*, The Copernicus Global 1/12° Oceanic and Sea Ice GLORYS12 Reanalysis. *Front Earth Sc-Switz* **9** (2021).
54. S. G. Yeager *et al.*, PREDICTING NEAR-TERM CHANGES IN THE EARTH SYSTEM A Large Ensemble of Initialized Decadal Prediction Simulations Using the Community Earth System Model. *B Am Meteorol Soc* **99**, 1867-1886 (2018).
55. S. M. Kang *et al.*, Km-scale coupled simulation and model–observation SST trend discrepancy. *Proceedings of the National Academy of Sciences* **123**, e2522161123 (2026).
56. P. R. Gent, J. C. Mcwilliams, Isopycnal Mixing in Ocean Circulation Models. *Journal of Physical Oceanography* **20**, 150-155 (1990).
57. S. W. Li, W. Liu, K. W. Lyu, X. B. Zhang, The effects of historical ozone changes on Southern Ocean heat uptake and storage. *Clim Dynam* **57**, 2269-2285 (2021).
58. S. Kravtsov, D. Kondrashov, I. Kamenkovich, M. Ghil, An empirical stochastic model of sea-surface temperatures and surface winds over the Southern Ocean. *Ocean Sci* **7**, 755-770 (2011).
59. L. W. O'Neill, D. B. Chelton, S. K. Esbensen, Observations of SST-induced perturbations of the wind stress field over the Southern Ocean on seasonal timescales. *J Climate* **16**, 2340-2354 (2003).
60. L. W. O'Neill, D. B. Chelton, S. K. Esbensen, The Effects of SST-Induced Surface Wind Speed and Direction Gradients on Midlatitude Surface Vorticity and Divergence. *J Climate* **23**, 255-281 (2010).
61. L. W. O'Neill, D. B. Chelton, S. K. Esbensen, Covariability of Surface Wind and Stress Responses to Sea Surface Temperature Fronts. *J Climate* **25**, 5916-5942 (2012).
62. N. Perlin, I. Kamenkovich, Y. Gao, B. P. Kirtman, A study of mesoscale air-sea interaction in the Southern Ocean with a regional coupled model. *Ocean Modelling* **153** (2020).
63. F. O. Bryan *et al.*, Frontal Scale Air-Sea Interaction in High-Resolution Coupled Climate Models. *J Climate* **23**, 6277-6291 (2010).
64. D. B. Chelton *et al.*, Observations of coupling between surface wind stress and sea surface temperature in the eastern tropical Pacific. *J Climate* **14**, 1479-1498 (2001).
65. D. B. Chelton, M. G. Schlax, M. H. Freilich, R. F. Milliff, Satellite measurements reveal persistent small-scale features in ocean winds. *Science* **303**, 978-983 (2004).
66. D. B. Chelton, S. P. Xie, Coupled Ocean-Atmosphere Interaction at Oceanic Mesoscales. *Oceanography* **23**, 52-69 (2010).
67. S. P. Hayes, M. J. Mcphaden, J. M. Wallace, The Influence of Sea-Surface Temperature on Surface Wind in the Eastern Equatorial Pacific - Weekly to Monthly Variability. *J Climate* **2**, 1500-1506 (1989).
68. R. J. Small, S. P. Xie, Y. Q. Wang, S. K. Esbensen, D. Vickers, Numerical simulation of boundary layer structure and cross-equatorial flow in the Eastern Pacific. *J Atmos Sci* **62**, 1812-1830 (2005).
69. J. M. Wallace, T. P. Mitchell, C. Deser, The Influence of Sea-Surface Temperature on Surface Wind in the Eastern Equatorial Pacific - Seasonal and Interannual Variability. *J Climate* **2**, 1492-1499 (1989).

70. R. S. Lindzen, S. Nigam, On the Role of Sea-Surface Temperature-Gradients in Forcing Low-Level Winds and Convergence in the Tropics. *J Atmos Sci* **44**, 2418-2436 (1987).
71. S. Minobe, A. Kuwano-Yoshida, N. Komori, S. P. Xie, R. J. Small, Influence of the Gulf Stream on the troposphere. *Nature* **452**, 206-U251 (2008).
72. M. A. Spall, Midlatitude wind stress-sea surface temperature coupling in the vicinity of oceanic fronts. *J Climate* **20**, 3785-3801 (2007).
73. F. Ogawa, N. E. Omrani, K. Nishii, H. Nakamura, N. Keenlyside, Ozone-induced climate change propped up by the Southern Hemisphere oceanic front. *Geophys Res Lett* **42**, 10056-10063 (2015).
74. J. Lu, G. Chen, D. M. W. Frierson, The Position of the Midlatitude Storm Track and Eddy-Driven Westerlies in Aquaplanet AGCMs. *J Atmos Sci* **67**, 3984-4000 (2010).
75. T. Sampe, H. Nakamura, A. Goto, W. Ohfuchi, Significance of a Midlatitude SST Frontal Zone in the Formation of a Storm Track and an Eddy-Driven Westerly Jet. *J Climate* **23**, 1793-1814 (2010).
76. B. Huang *et al.*, Extended Reconstructed Sea Surface Temperature, Version 5 (ERSSTv5): Upgrades, Validations, and Intercomparisons. *J Climate* **30**, 8179-8205 (2017).
77. B. Huang *et al.*, NOAA Extended Reconstructed Sea Surface Temperature (ERSST), Version 5. National Oceanic and Atmospheric Administration. https://psl.noaa.gov/data/gridded/data.noaa.ersst.v5.html. http://doi.org/10.7289/V5T72FNM. Accessed 15 March 2026.
78. H. Hersbach *et al.*, The ERA5 global reanalysis. *Q J Roy Meteor Soc* **146**, 1999-2049 (2020).
79. H. Hersbach *et al.*, European Centre for Medium-Range Weather Forecasts, ERA5 monthly averaged data on single levels from 1940 to the present. https://cds.climate.copernicus.eu/datasets/reanalysis-era5-single-levels-monthly-means?tab=overview. http://doi.org/10.24381/cds.f17050d7. Accessed 15 March 2026.
80. R. F. Adler *et al.*, The Global Precipitation Climatology Project (GPCP) Monthly Analysis (New Version 2.3) and a Review of 2017 Global Precipitation. *Atmosphere* **9**, 138 (2018).
81. R. F. Adler *et al.*, Global Precipitation Climatology Project (GPCP) Climate Data Record (CDR), Version 2.3 (Monthly). https://www.ncei.noaa.gov/access/metadata/landing-page/bin/iso?id=gov.noaa.ncdc:C00979. http://doi.org/10.7289/V56971M6. Accessed 15 March 2026.
82. J.-M. Lellouche *et al.*, The Copernicus Global 1/12° Oceanic and Sea Ice GLORYS12 Reanalysis. https://data.marine.copernicus.eu/product/GLOBAL_MULTIYEAR_PHY_001_030/services. http://doi.org/10.48670/moi-00021. Accessed 15 March 2026.
83. F. Castruccio *et al.*, MESACLIP: A 500-year CESM HR pre-industrial control simulation forced with perpetual 1850 conditions. NSF National Center for Atmospheric Research. https://gdex.ucar.edu/datasets/d651029/. http://doi.org/10.5065/2K6J-SB78. Accessed 15 March 2026.
84. F. Castruccio *et al.*, MESACLIP: A 10-member ensemble of CESM HR historical (1920-2005) simulations. NSF National Center for Atmospheric Research https://gdex.ucar.edu/datasets/d651007/. http://doi.org/10.5065/7N1X-K278. Accessed 15 March 2026.
85. F. Castruccio *et al.*, MESACLIP: A 10-member ensemble of CESM HR RCP 8.5 (2006-2100) simulations. NSF National Center for Atmospheric Research. https://gdex.ucar.edu/datasets/d651009/. http://doi.org/10.5065/PNCR-5S34. Accessed 15 March 2026.
86. F. Castruccio *et al.*, MESACLIP: Nominal 1-degree CESM (low-resolution) simulations corresponding to high-resolution experiments. NSF National Center for Atmospheric Research. https://gdex.ucar.edu/datasets/d651030/. http://doi.org/10.5065/DBZQ-1K04. Accessed 15 March 2026.

87. M. J. Roberts *et al.*, Impact of Model Resolution on Tropical Cyclone Simulation Using the HighResMIP-PRIMAVERA Multimodel Ensemble. *J Climate* **33**, 2557-2583 (2020).
88. M. J. Roberts *et al.*, Projected Future Changes in Tropical Cyclones Using the CMIP6 HighResMIP Multimodel Ensemble. *Geophys Res Lett* **47** (2020).
89. J. Hurrel *et al.*, IPCC DDC: NCAR CESM1-CAM5-SE-HR model output prepared for CMIP6 HighResMIP. World Data Center for Climate (WDCC) at DKRZ. http://doi.org/10.26050/WDCC/AR6.C6HRNRCCS. Accessed 15 March 2026.
90. E. Scoccimarro *et al.*, Extreme events representation in CMCC-CM2 standard and high-resolution general circulation models. *Geosci Model Dev* **15**, 1841-1854 (2022).
91. E. Scoccimarro, A. Bellucci, D. Peano, CMCC CMCC-CM2-VHR4 model output prepared for CMIP6 HighResMIP. Earth System Grid Federation. http://doi.org/10.22033/ESGF/CMIP6.1367. Accessed 15 March 2026.
92. R. Haarsma *et al.*, HighResMIP versions of EC-Earth: EC-Earth3P and EC-Earth3P-HR - description, model computational performance and basic validation. *Geosci Model Dev* **13**, 3507-3527 (2020).
93. R. Haarsma *et al.*, EC-Earth-Consortium EC-Earth3P-HR model output prepared for CMIP6 HighResMIP. Earth System Grid Federation. http://doi.org/10.22033/ESGF/CMIP6.2323. Accessed 15 March 2026.
94. M. J. Roberts *et al.*, Description of the resolution hierarchy of the global coupled HadGEM3-GC3.1 model as used in CMIP6 HighResMIP experiments. *Geosci Model Dev* **12**, 4999-5028 (2019).
95. M. Roberts, MOHC HadGEM3-GC31-HH model output prepared for CMIP6 HighResMIP. Earth System Grid Federation. http://doi.org/10.22033/ESGF/CMIP6.445. Accessed 15 March 2026.
96. O. Gutjahr *et al.*, Max Planck Institute Earth System Model (MPI-ESM1.2) for the High-Resolution Model Intercomparison Project (HighResMIP). *Geosci Model Dev* **12**, 3241-3281 (2019).
97. J.-S. von Storch *et al.*, MPI-M MPI-ESM1.2-XR model output prepared for CMIP6 HighResMIP. Earth System Grid Federation. http://doi.org/10.22033/ESGF/CMIP6.10290. Accessed 15 March 2026.
98. R. J. Haarsma *et al.*, High Resolution Model Intercomparison Project (HRMIP). https://esgf-node.llnl.gov/projects/cmip6/. Accessed 15 March 2026.
99. J. E. Kay, C. Deser, A. S. Phillips, I. R. Simpson, CESM1 Large Ensemble Community Project. NSF National Center for Atmospheric Research. https://gdex.ucar.edu/datasets/d651027/. http://doi.org/10.5065/D6J101D1. Accessed 15 March 2026.
100. N. A. Rayner *et al.*, Global analyses of sea surface temperature, sea ice, and night marine air temperature since the late nineteenth century - art. no. 4407. *J Geophys Res-Atmos* **108** (2003).
101. N. A. Rayner *et al.*, Hadley Centre Global Sea Ice and Sea Surface Temperature (HadISST). NSF National Center for Atmospheric Research. https://gdex.ucar.edu/datasets/d277003/. http://doi.org/10.5065/XMYE-AN84. Accessed 15 March 2026.

Figures

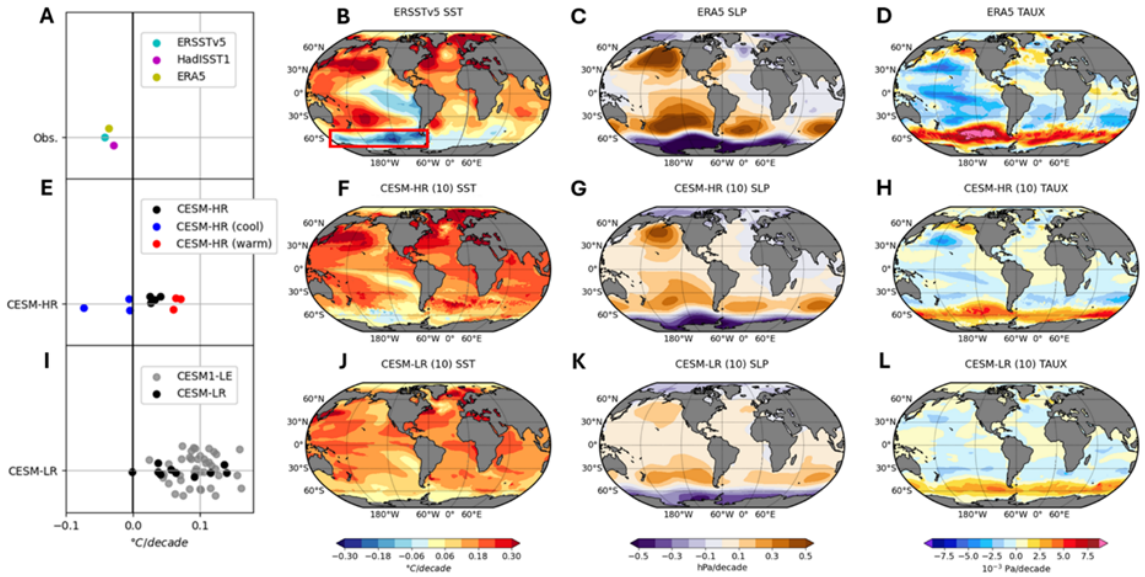

Figure 1. Observation-based and simulated linear trends of SST, SLP, and τ_x over the period 1980-2022. Linear trends of observed SST averaged in the South Pacific region of the Southern Ocean indicated by the red box region in panel B for (A) ERSSTv5, HadISST, and ERA5, (E) CESM-HR, and (I) CESM-LR and CESM1-LE. Spatial map of linear trends in observation-based products (ERSSTv5 or ERA5) for SST, SLP, and τ_x are shown in (B), (C), and (D), respectively. The ensemble-mean linear trends in CESM-HR for SST, SLP, and τ_x are shown in (F), (G), and (H), respectively. The ensemble-mean linear trends in CESM-LR for SST, SLP, and τ_x are shown in (J), (K), and (L), respectively. For the CESM-HR SST trends in (E), the 3 coldest members are indicated in blue, the 3 warmest in red, and the remaining 4 in black.

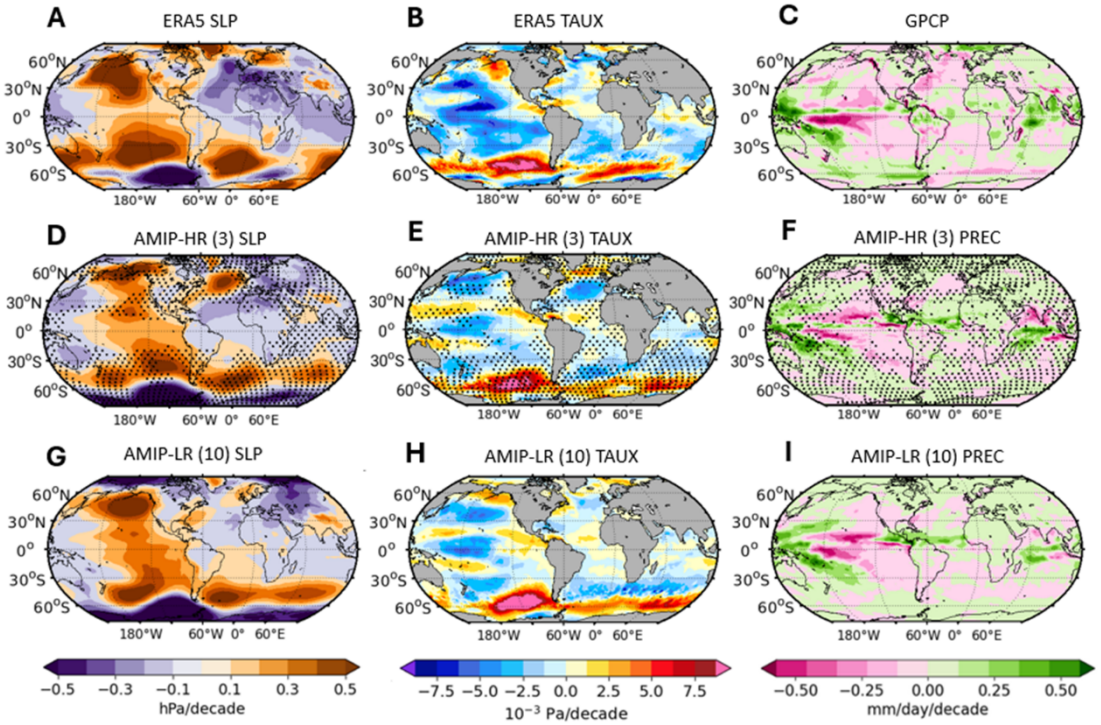

Figure 2. Observation-based and simulated linear trends of SLP, τ_x, and precipitation over 1980-2014. Trends in ERA5 of (A) SLP and (B) τ_x, and trends of precipitation from (C) GPCP. Trends in AMIP-HR for (D) SLP, (E) τ_x, and (F) precipitation. Trends in AMIP-LR for (G) SLP, (H) τ_x, and (I) precipitation. AMIP-HR has 3 ensemble members and AMIP-LR has 10 ensemble members. Stippling in the AMIP-HR panels (D–F) indicates regions where the 3-member AMIP-HR trend lies within the 5–95% percentile range of a bootstrapped distribution constructed from 3-member means of the 10-member AMIP-LR ensemble, indicating no statistically significant difference between AMIP-HR and AMIP-LR.

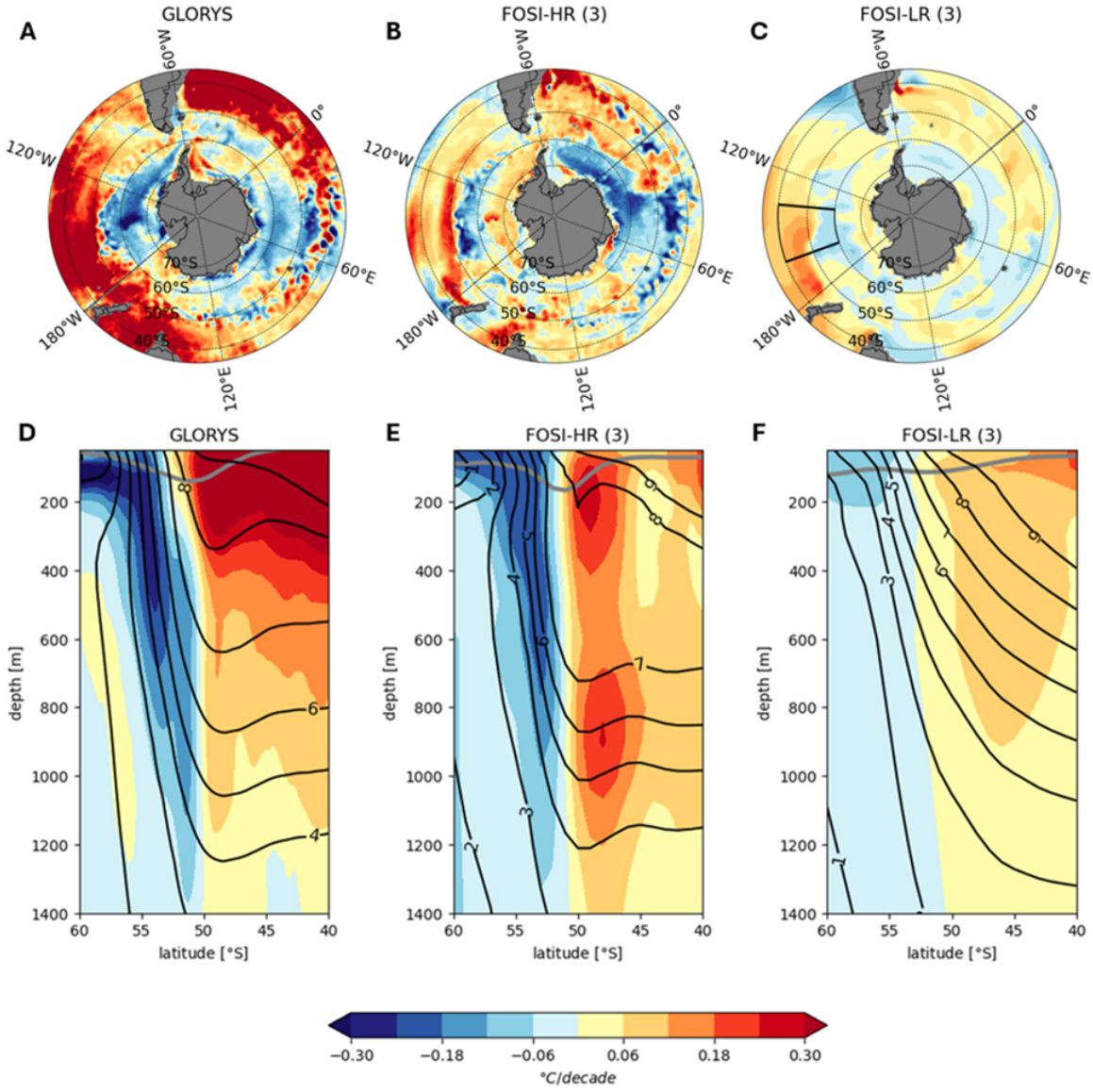

Figure 3. Linear trends of upper ocean temperature in reanalysis (GLORYS) and FOSI. Linear trend of ocean temperature averaged between 100-500 m in (A) GLORYS, (B) FOSI-HR, and (C) FOSI-LR. Linear trend (color) and mean (black contours) of ocean temperature over a vertical slice averaged across 160°W-145°W (indicated by the black box in panel C) in (D) GLORYS, (E) FOSI-HR, and (F) FOSI-LR. FOSI mean and linear trends are calculated over the period 1979-2017. GLORYS mean and linear trends are calculated over the period 1993-2017. The mean and linear trends of the FOSI simulations over the overlapping period with GLORYS (1993-2017) are comparable to the full period 1979-2017. The mean MLD over the same longitudinal slice is indicated by the gray lines in each panel.

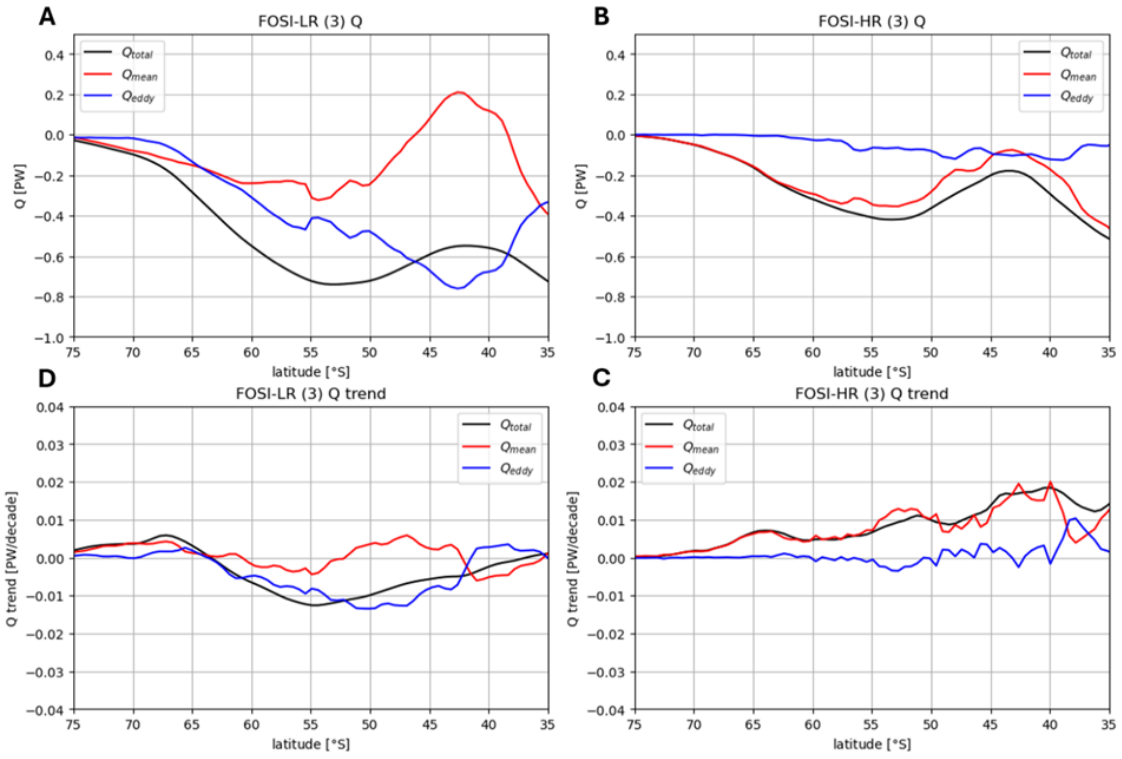

Figure 4. Southern Ocean meridional heat transport (Q) in FOSI-HR and FOSI-LR over the 1979-2017 period. The upper panels show the climatological mean Q_{total} (black curves) and its Eulerian mean (Q_{mean}; red curves)) and transient eddy (Q_{eddy}; blue curves) components for (A) FOSI-LR and (B) FOSI-HR. The lower panel show the linear trends in these quantities for (C) FOSI-LR and (D) FOSI-HR.

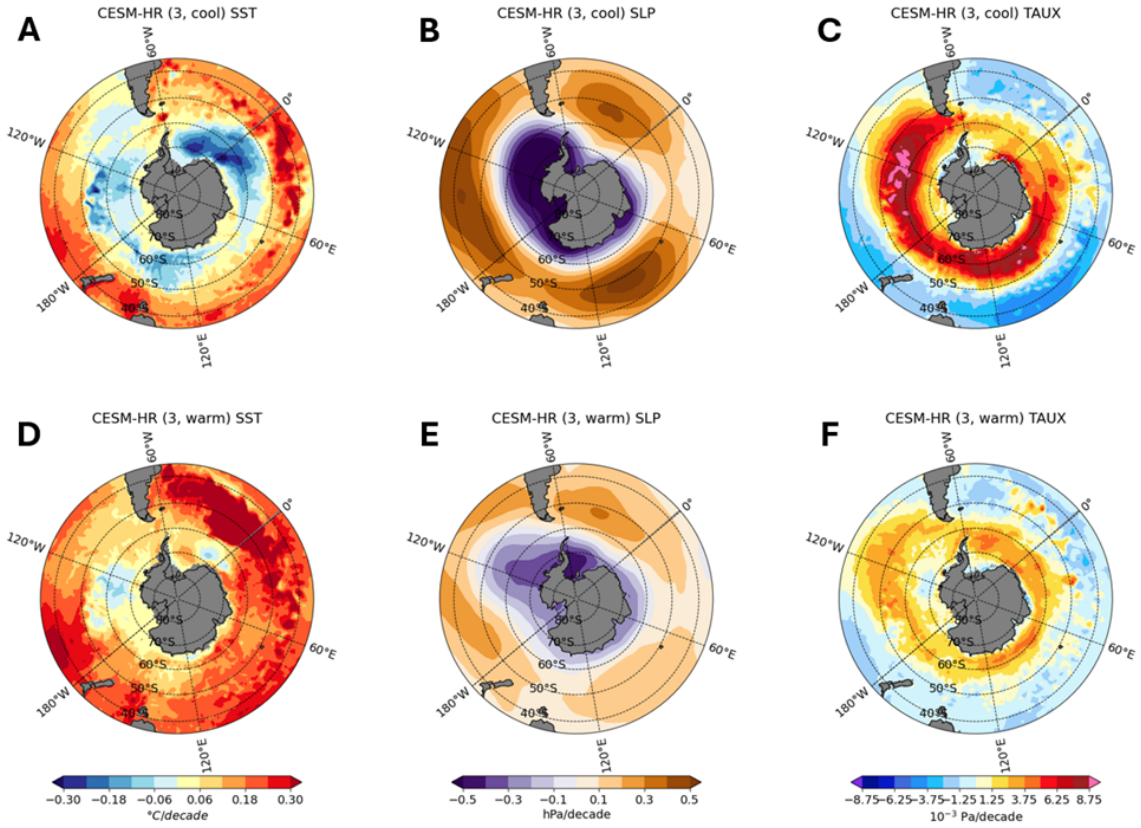

Figure 5. Linear trends of SST, SLP, and τ_x in CESM-HR over the 1980-2022 period, averaged across ensemble members with cooling or warming in the South Pacific sector of the Southern Ocean. The upper panels show the mean of the 3 members with cooling for (A) SST, (B) SLP, and (C) τ_x. The lower panels show the mean of the 3 members with strongest warming for (D) SST, (E) SLP, and (F) τ_x.

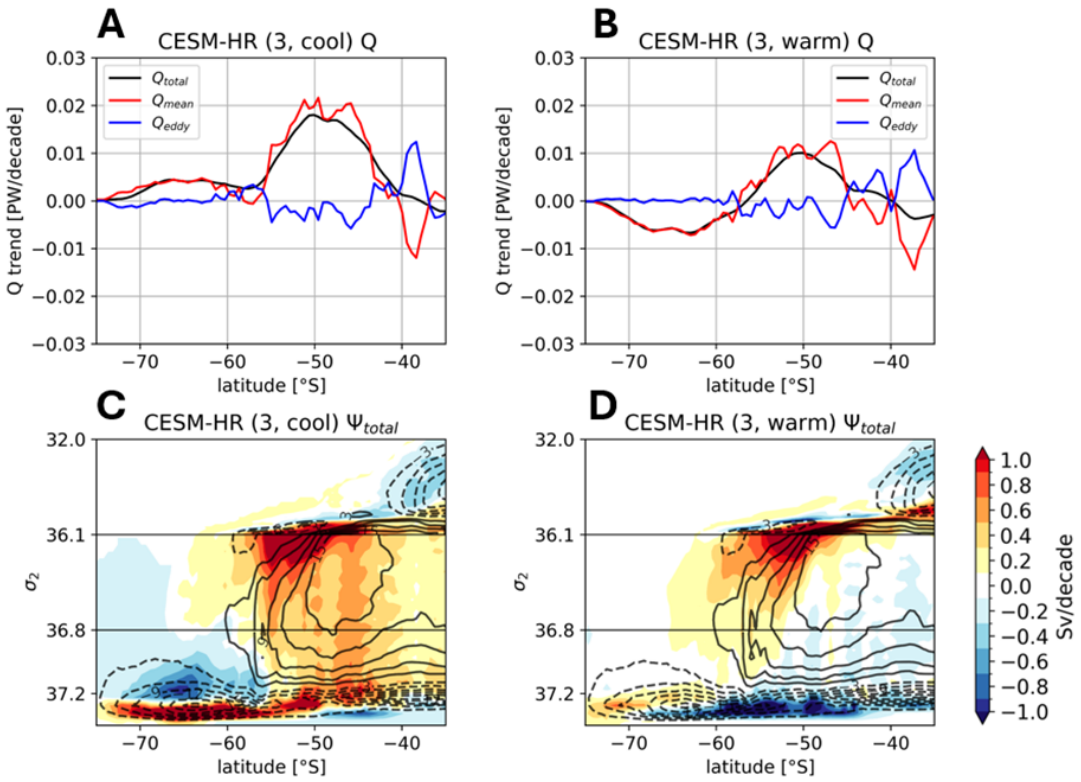

Figure 6. Linear trends of meridional heat transport (Q) and time-mean and linear trends of residual overturning streamfunction (Ψ_{total}) in density space from CESM-HR over the 1980-2022 period. In the upper panels, trends in Q averaged across ensemble members with (A) SST cooling (3-member mean, "cool") and (B) SST warming (3-member mean, "warm"). In the lower panels, Ψ_{total} mean (contours, 5 Sv intervals) and trends (shading) averaged across ensemble members with (C) SST cooling (3-member mean, "cool") and (D) SST warming (3-member mean, "warm").

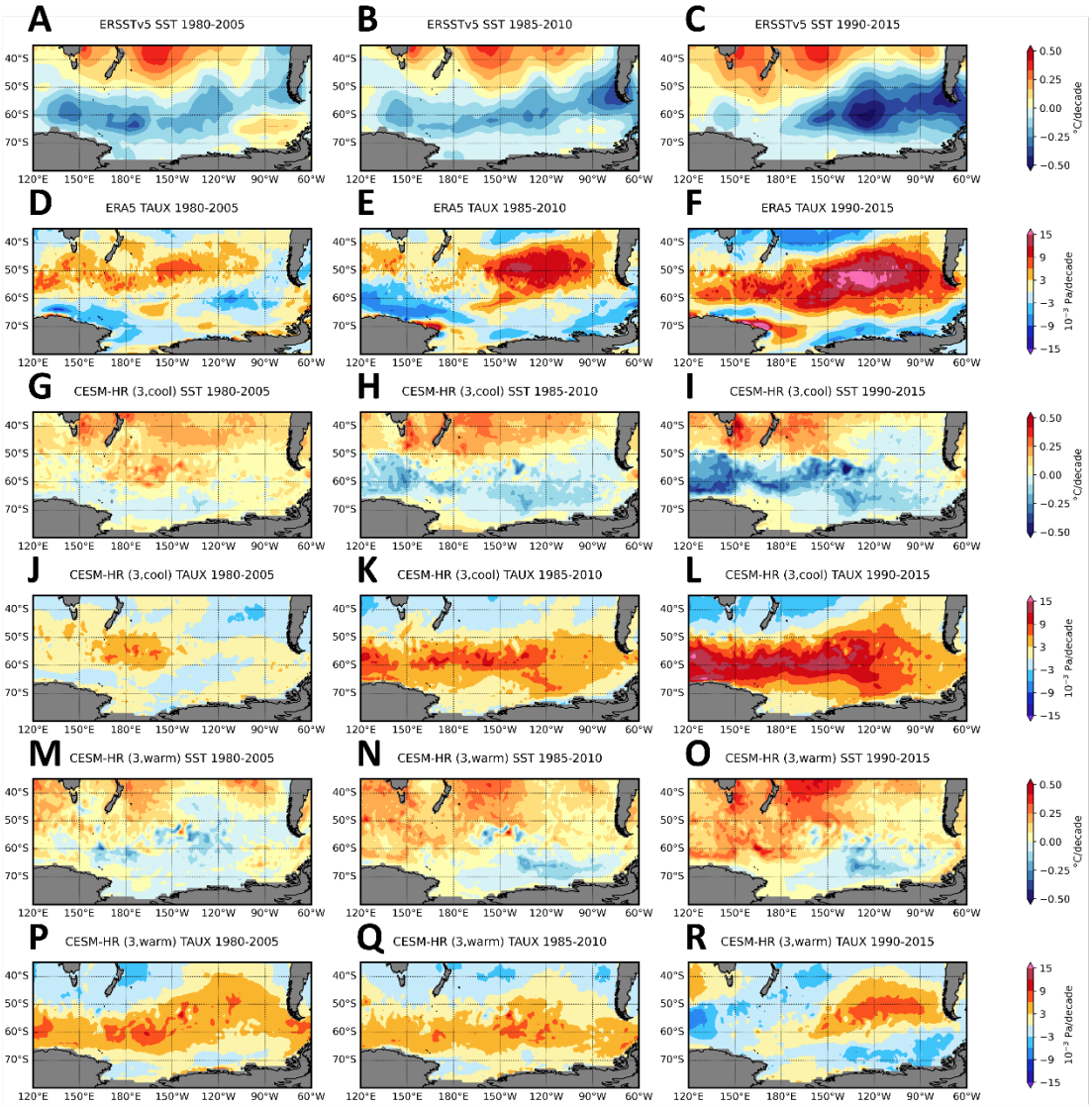

Fig. 7: Linear trends of SST and zonal surface wind stress in ERSSTv5, ERA5, and the CESM-HR cool and warm groups computed for three windows over the 1980-2015 period, with each of the three panel columns indicating 1980-2005, 1985-2010, and 1990-2015, respectively. (A, B, C) ERSSTv5 SST (D, E, F) ERA5 τ_x, (G, H, I) CESM-HR cool group SST, (J, K, L) CESM-HR cool group τ_x, (M, N, O) CESM-HR warm group SST, and (P, Q, R) CESM-HR warm group τ_x.